

# Versatile and reconfigurable integrated silicon nitride photonic microresonator

Tong Lin,<sup>a,b,†,\*</sup> Haoran Wang,<sup>a,†</sup> Xiaoyu Hao,<sup>a,†</sup> Liu Li,<sup>c</sup> Ziyang Xiong,<sup>a</sup> Hao Deng,<sup>a</sup> Yan Fan,<sup>a</sup> Shihua Chen,<sup>d</sup> Junpeng Lu<sup>a</sup>, Zhenhua Ni<sup>a,d</sup>

<sup>a</sup>Southeast University, Photonic integrated circuits & systems group, School of Electronic Science and Engineering, No. 2 Southeast University Road, Jiangning District, Nanjing, China

<sup>b</sup>Key Lab of Modern Optical Technologies of Education Ministry of China, Soochow University, No.1 Shizi Street, Suzhou, China

<sup>c</sup>Southeast University, School of Material Science and Engineering, No. 2 Southeast University Road, Jiangning District, Nanjing, China

<sup>d</sup>Southeast University, Advanced Ocean Institute, No. 2 Southeast University Road, Jiangning District, Nantong, China

**Abstract.** Unlocking the full potential of integrated photonics requires versatile, multi-functional devices that can adapt to diverse application demands. However, confronting this challenge with conventional single-function resonators often results in **cumbersome system designs**. We present an elegant solution: a versatile and reconfigurable dual-polarization Si<sub>3</sub>N<sub>4</sub> microresonator that **represents a new perspective in on-chip photonic designs**. **Our device can be dynamically reconfigured into three distinct topologies**: a Möbius-like microcavity, a Fabry-Pérot resonator, and a microring resonator. This unprecedented functionality is enabled by a tunable balanced Mach-Zehnder interferometer that facilitates controllable mutual mode coupling of counterpropagating lights using a single control knob. **We experimentally demonstrate that the device not only supports polarization-diverse operation on a footprint but also gives rise to a rich variety of physical phenomena, including a standing wave cavity, a traveling wave cavity, free spectral range multiplication, and the photonic pinning effect**. These behaviors are accurately modeled using the Transfer Matrix Method and intuitively explained by Temporal Coupled Mode Theory. Our results underscore the potential for a chip-scale platform to realize reconfigurable reconstructive spectrometers and on-chip synthetic dimensions for topological physics.

**Keywords:** Silicon nitride, optical cavity, reconfigurable photonics, microring resonator, Fabry-Pérot resonator, polarization diversity.

<sup>†</sup>Tong Lin, Haoran Wang, and Xiaoyu Hao contributed equally to this work.

\*Tong Lin, E-mail: lintong@seu.edu.cn

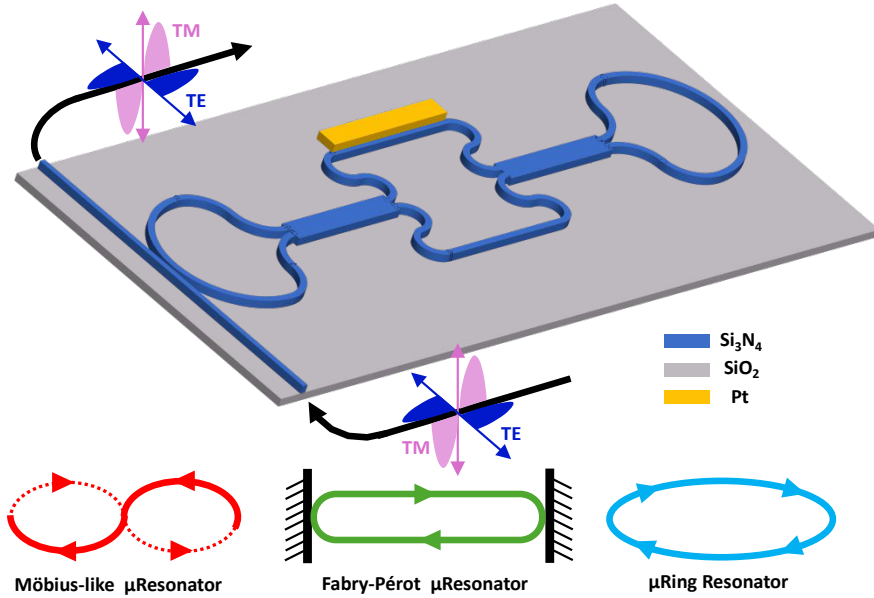
## 33 1 Introduction

34 Integrated photonic microresonators<sup>1</sup> have become a cornerstone technology for the  
35 miniaturization and mass production of optical components, with broad applications in high-speed  
36 optical communications,<sup>2, 3</sup> photonic computing,<sup>4, 5</sup> chemical sensing,<sup>6</sup> biomedical diagnostics,<sup>7</sup>  
37 and quantum information processing.<sup>8</sup> Their appeal lies in compact form factors, high quality  
38 factors, and strong light–matter interactions. However, the field remains constrained by a  
39 fundamental limitation: conventional photonic resonators are inherently single-function devices.  
40 Without extensive circuit-level redesign, they cannot adapt to varying application demands. This  
41 architectural rigidity hinders the development of versatile on-chip systems that require  
42 reconfigurable spectral control, multifunctional operation, and polarization diversity within a  
43 minimal footprint.

44 In recent years, significant research efforts have focused on developing reconfigurable  
45 integrated microresonators, primarily leveraging interferometric designs to manipulate optical  
46 pathways. In bulk optical systems, aligning even a few interferometric elements remains  
47 challenging. Advances in micro/nanofabrication now enable the monolithic integration of complex  
48 photonic circuits, leading to diverse approaches such as: reconfigurable optical gates based on  
49 hexagonal cells,<sup>1, 9</sup> double-injection resonators,<sup>10, 11</sup> networks of microring resonators (MRRs),<sup>12,</sup>  
50 <sup>13</sup> cascaded Mach–Zehnder interferometers (MZIs),<sup>14</sup> and hybrid structures of Mach–Zehnder  
51 interferometers and MRRs.<sup>15-17</sup> **Despite enabling sophisticated spectral shaping, these methods**  
52 **universally rely on intricate photonic circuitry and multi-channel electrical control schemes—**  
53 **resulting in cumbersome designs and computationally intensive operation. Moreover, as the**  
54 **footprint of the photonic components is shared with their electrical control interfaces, the number**  
55 **of electrical channels becomes a limiting factor in scaling up functional complexity. As a result, a**  
56 **fundamentally distinct solution, one versatile microresonator with single-knob reconfigurability,**  
57 **is thus critically needed to advance programmable photonics.**

58 In this work, we bridge this critical gap by introducing a versatile reconfigurable dual-  
59 polarization silicon nitride ( $\text{Si}_3\text{N}_4$ ) microresonator. We demonstrate that this single device can be  
60 dynamically reconfigured into three distinct operational modes—a Möbius-like microcavity,<sup>18</sup> a  
61 Fabry-Pérot resonator, and a MRR—enabling unprecedented multi-functionality on chip using a  
62 single control knob. Furthermore, our design benefits from the use of an 0.8- $\mu\text{m}$  thick  $\text{Si}_3\text{N}_4$   
63 photonic platform, which is engineered to minimize birefringence and support polarization

64 diversity. The cavity dynamics are accurately modeled by the transfer matrix method (TMM) and  
 65 intuitively explained by the temporal coupled mode theory (TCMT). Through experiment  
 66 validations, we further unveil a suite of intriguing physical phenomena intrinsic to this platform,  
 67 including free spectral range (FSR) multiplication and the photonic pinning effect. Our findings  
 68 not only provide a versatile building block for programmable photonic circuits but also open new  
 69 pathways toward on-chip synthetic dimensions and **reconstructive** spectroscopic systems.<sup>19</sup>



70  
 71 **Fig. 1** The artistic view of the proposed reconfigurable dual-polarization  $\text{Si}_3\text{N}_4$  microresonator, supporting three  
 72 distinctive resonators.

73 **2 Reconfigurable Photonic Microresonator**

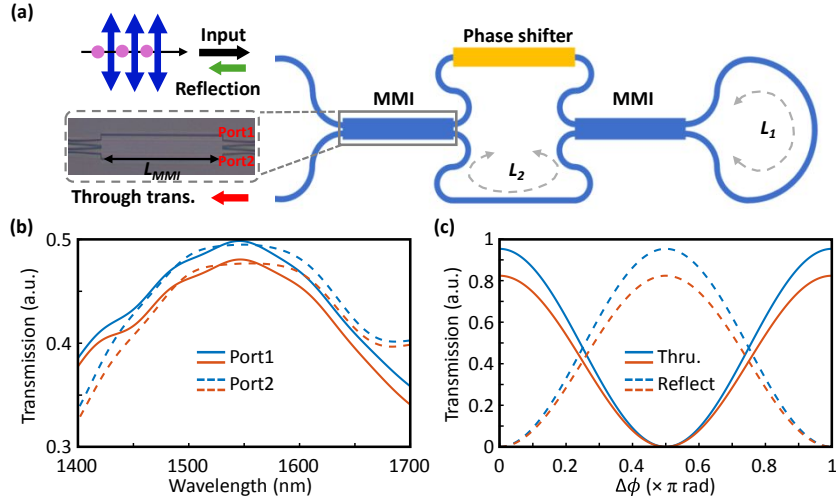
74 We present a reconfigurable dual-polarization  $\text{Si}_3\text{N}_4$  microresonator, leveraging a novel optical  
 75 architecture capable of dynamically switching between three distinct resonator configurations. As  
 76 illustrated in Fig. 1, **the proposed device features a resonant loop**, side-coupled to a bus waveguide  
 77 for optical input and output. **This loop is formed by interconnecting two identical Sagnac-loop**  
 78 **reflectors in a port-to-port configuration.** Each reflector is constructed using a  $2 \times 2$  multimode  
 79 **interferometer (MMI) whose two output ports are looped back to form a closed path.** Phase control  
 80 is achieved via the thermo-optic effect using an integrated microheater atop one of the connecting  
 81 waveguides. The core of the microresonator can also be viewed as a tunable balanced MZI, which  
 82 facilitates controllable mutual mode coupling. The resulting optical paths—incorporating intricate  
 83 reflection and transmission dynamics within the resonant structure—give rise to a rich variety of

84 physical phenomena, i.e., standing wave cavity, traveling wave cavity, FSR multiplication, and  
85 photonic pinning effect. Fabricated on a  $\text{Si}_3\text{N}_4$ -on-insulator platform,<sup>20</sup> the  $\text{Si}_3\text{N}_4$  microresonator  
86 enables a straightforward polarization-diverse operation in a manner, making it suitable for  
87 advanced integrated photonic applications.

## 88 2.1 Architecture of the Photonic Router

89 To achieve dual-polarization reconfigurability, we implement a tunable Sagnac reflector as the  
90 core on-chip photonic router, leveraging polarization insensitive interferometric design. Figure 2(a)  
91 schematically illustrates this router, which employs polarization insensitive MMIs and a thermo-  
92 optic phase shifter to dynamically regulate optical paths. Structurally, the photonic router functions  
93 as a balanced MZI with interconnected outputs—akin to a drop shape with a perimeter of about  
94  $634.16\ \mu\text{m}$  ( $L_1$ ). Within the MZI, two  $2\times 2$  MMIs are interconnected port-to-port via S-bends, each  
95 spanning  $634.92\ \mu\text{m}$  ( $L_2$ ) with four  $180^\circ$  circular bends ( $25\ \mu\text{m}$  radius). The MMI operates on the  
96 self-imaging principle to equally split incident light. We optimize MMI performance using finite-  
97 difference time-domain (FDTD) simulations (Ansys Lumerical Inc.). Equalizing the beat lengths  
98 for both polarizations yields polarization-insensitive operation with a central multimode body  
99 cross-section of  $130\ \mu\text{m}\times 12.6\ \mu\text{m}$ . At multimode interfaces, pairs of  $3\text{-}\mu\text{m}$ -wide waveguides ( $1.2$   
100  $\mu\text{m}$  lateral spacing) are adiabatically tapered to  $1\ \mu\text{m}$  width over  $40\ \mu\text{m}$  lengths longitudinally.  
101 While non-tapered waveguides maintain  $1\ \mu\text{m}$  width, the entire waveguide layer is  $0.8\ \mu\text{m}$  thick.

102 Figures 2(b)–(c) validate near-identical MMI output transmissions for TE and TM modes. At  
103  $1550\ \text{nm}$ , both output branches achieve  $49.65\pm 0.20\%$  transmission efficiency for TE polarization,  
104 while TM polarization exhibits slightly higher insertion loss with peak efficiency at  $47.85\pm$   
105  $0.20\%$ . Using Ansys Lumerical INTERCONNECT, we simulate the Sagnac reflector's tunable  
106 response. Figures 2(d–e) plot transmission (solid blue) and reflection (dashed blue) spectra versus  
107 phase shift  $\Delta\phi$ . For TE input (Fig. 2(d)), the reflector operation occurs at  $\Delta\phi=0.5\pi$ , where  
108 reflection approaches unity and transmission minimizes. For TM input (Fig. 2(e)), peak reflection  
109 reduces to 80% at  $\Delta\phi=0.5\pi$  due to MMI insertion loss. At  $\Delta\phi=0$  or  $\pi$ , the device functions as an  
110 all-pass filter with  $95.3\pm 0.1\%$  transmission through the lower port. As the wide range phase shift  
111 is readily attained with thermal-optic tuning, these simulation results confirm tunable routing  
112 capability of the constructed reflector.



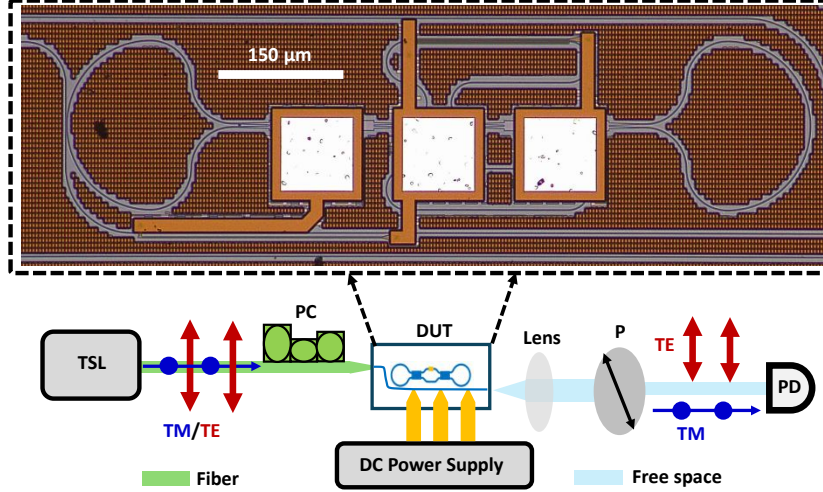
113

114 **Fig. 2** (a) The schematic of the tunable Sagnac reflector as the photonic router ( $L_{\text{MMI}}=130 \mu\text{m}$ ). The inset is one optical  
 115 microscope image of the fabricated MMI. (b) Simulated two port transmission spectra of a polarization-insensitive  
 116 MMI for TE mode (blue line) and TM mode (orange line). (c) Simulated reflection and transmission spectra of the  
 117 constructed Sagnac reflector for TE mode (blue line) and TM mode (orange line).

### 118 3 Experimental Results and Discussion

#### 119 3.1 Experimental Implementation

120 We experimentally demonstrate the reconfigurability of the fabricated photonic device for both  
 121 TE and TM polarizations. The device was manufactured on a commercial  $\text{Si}_3\text{N}_4$  photonics  
 122 platform (Ligentec Inc.). A microscope image of the structure is provided in the top inset of Fig.  
 123 3. The  $\text{Si}_3\text{N}_4$  waveguide features nearly vertical sidewalls ( $89^\circ$  sidewall angle) **according to the**  
 124 **foundry manufacturer; this characteristic contributes to negligible birefringence for the**  
 125 **waveguides with a cross-section of  $1 \mu\text{m} \times 0.8 \mu\text{m}$ .** For optical characterization, light from a tunable  
 126 laser is coupled into the device under test (DUT) via a lensed fiber, as depicted in Fig. 3. The  
 127 output light is collimated using an aspheric lens and passed through a free-space polarizer. By  
 128 rotating the polarizer, we selectively measure the transmission spectra for TE and TM polarizations  
 129 using a photodetector. Reconfigurability is achieved via integrated microheaters, positioned  $3.3$   
 130  $\mu\text{m}$  above the waveguides, enabling efficient phase tuning of the photonic router.



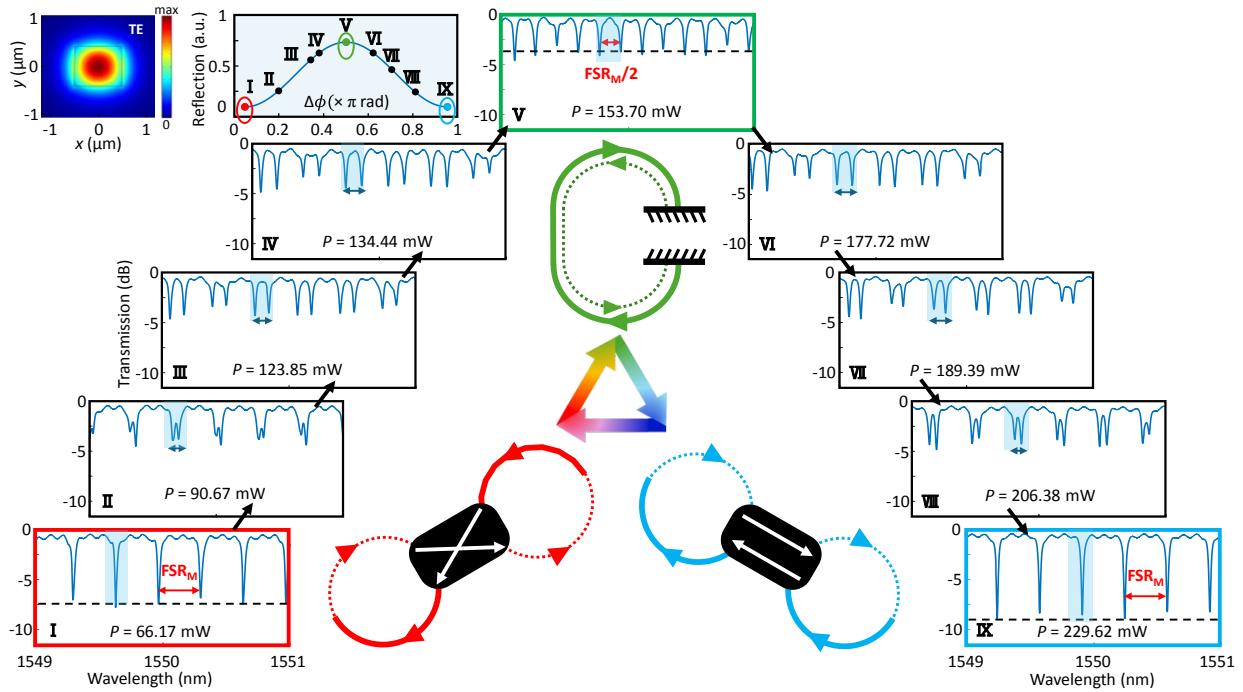
131  
132  
133  
134  
135

**Fig. 3** The optical microscope image of the fabricated device and the experimental apparatus for characterizing its reconfigurable optical properties: TSL (Santec TLS-570), PC (Polarization controller), DC power supply (Keysight 33522B), P (OPPF05-NIR, JCOPTIX), PD (Santec MPM-210).

### 136 3.2 Reconfigurability and Spectral Evolution

137 We experimentally demonstrate the reconfigurable functionality of the device for both TE and TM  
138 polarizations. The observed behavior is well captured by TMM simulations (see Sec. S1 in the  
139 Supplementary Material for details). The reconfiguration mechanism relies critically on the  
140 tunable reflection introduced by the photonic router. **From experimental transmission spectra, we**  
141 **extract the reflectivity as a function of the applied phase shift  $\Delta\phi$ , which exhibits a period of  $\pi$ .**  
142 **For TE-polarized input, nine distinct states are identified, corresponding to the labeled points on**  
143 **the reflection curve in the top-left panel of Fig. 4.** In State I, the resonator operates in a Möbius-  
144 like topology due to the cross-intersection behavior of the photonic router at zero phase shift. This  
145 unidirectional loop structure, with its characteristic one-sided topology, defines an optical path  
146 length  $L$  ( $L=2L_1+2L_2+4L_{MMI}$ ), yielding a FSR of about 0.3389 nm, consistent with the theoretical  
147 value:  $FSR=c/(n_g L)$ . The presence of non-zero bias power results from fabrication-induced arm  
148 imbalance in the interferometer, a common feature in integrated MZIs.<sup>21</sup> As the applied power  
149 increases from State II to State IV, enhanced reflection from the photonic router leads to  
150 progressively larger mode splitting. **At peak reflectivity, the router acts as a bidirectional reflector,**  
151 **effectively emulating a standing-wave Fabry–Pérot cavity with two end mirrors—as illustrated in**  
152 **the green inset.** The corresponding FSR is halved to 0.1697 nm, matching the canonical Fabry–

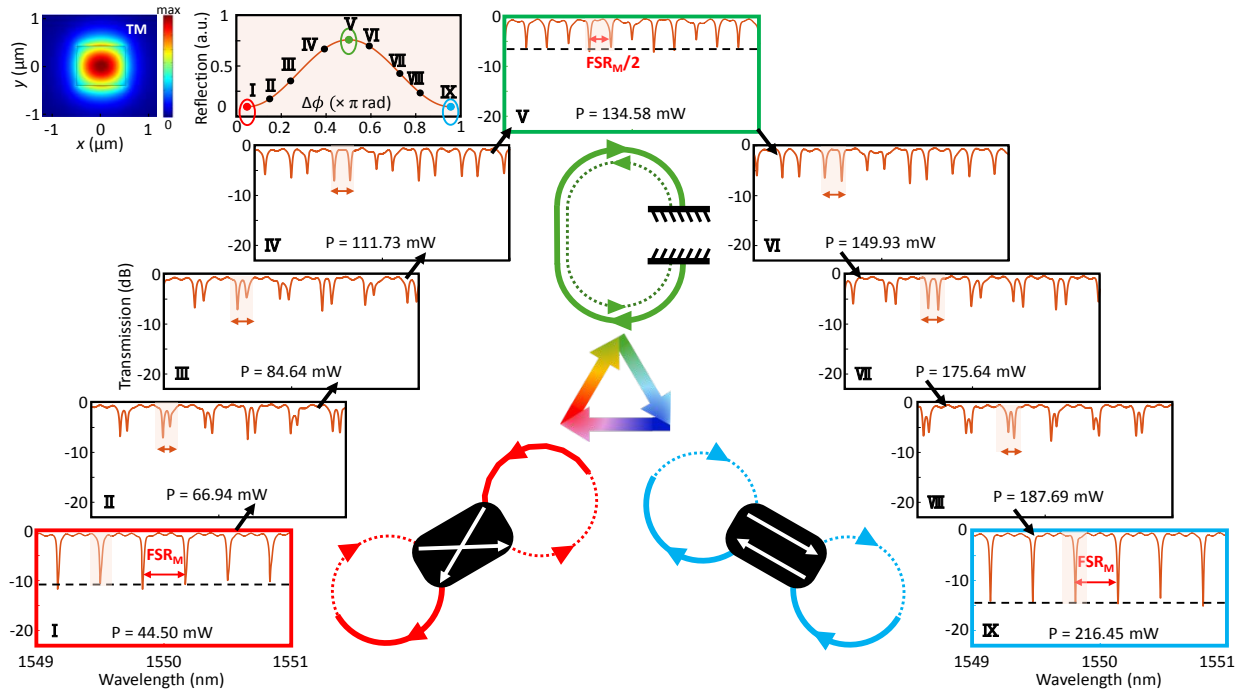
153 Pérot formula:  $FSR=c/(2n_gL)$ . Beyond 153.7 mW, reflectivity decreases monotonically, reducing  
 154 the mode splitting through States VI to VIII. Notably, at a  $\pi$  phase shift, the photonic router enters  
 155 the “bar” state, enabling microring-type resonance. In State IX, the measured FSR is  
 156 approximately 0.3345 nm—nearly identical to the Möbius-like case—as the optical path length  
 157 remains unchanged. Variations in extinction ratios (ERs) across states are attributed to insertion  
 158 loss differences between the “on” and “off” states of the MZI, arising primarily from the  $2\times 2$  MMI  
 159 imbalance.



160  
 161 **Fig. 4** The spectral evolutions of the reconfigurable  $\text{Si}_3\text{N}_4$  microresonator for TE-polarized input with the wavelength  
 162 spanning from 1549 nm to 1551 nm by altering the applied electrical power ( $P$ ). Among them, the red, green, and blue  
 163 bold wireframe correspond to three distinct states of the microresonator respectively (State I: a Möbius-like  
 164 microcavity, State V: a Fabry-Pérot resonator, State IX: a MRR). The spectra with black wireframe represent the  
 165 transition states between three states. The top left panel shows the simulated fundamental TE mode profile ( $n_g \sim 2.0863$ )  
 166 and the reflectivity versus the applied phase shift, derived from all the measured spectra.

167 Our measurements for TM-polarized input confirm the same full range of reconfigurable  
 168 functionality, providing compelling evidence of the device's robust performance and polarization-  
 169 insensitive operation. Similarly, Figure 5 depicts the transmission spectral evolutions as the  
 170 electrical tuning power increases from 44.5 mW to 216.45 mW. In State I, the resonator exhibits  
 171 Möbius-like behavior with a FSR of approximately 0.3352 nm. The slight discrepancy between  
 172 TE and TM FSR values stems from a group index difference of  $6 \times 10^{-3}$  between the two

173 fundamental modes. In State V, the Fabry–Pérot resonance becomes dominant, exhibiting a nearly  
 174 halved FSR of about 0.1706 nm. The thermal tuning power slightly deviates from the value  
 175 required for peak reflection, resulting in a minor FSR offset of only 5 pm. The dynamic evolution  
 176 stops manually in State IX, where the resonator is reconfigured as a MRR with a well-defined FSR  
 177 of about 0.3337 nm and comparatively higher ERs, consistent with the behavior explained earlier.  
 178 Interestingly, the loaded Q-factors for the TM mode are higher than those for TE, despite the larger  
 179 simulated insertion loss of the TM-polarized MMI (Figs. 2(b–c)). **This enhancement may be due**  
 180 **to the lower propagation loss of the TM mode and we will investigate this issue in the future.**



181  
 182 **Fig. 5** The spectral evolutions of the reconfigurable  $\text{Si}_3\text{N}_4$  microresonator for the TM-polarized input with the  
 183 wavelength spanning from 1549 nm to 1551 nm by altering the applied electrical power (P). Among them, the red,  
 184 green, and blue bold wireframe correspond to three distinct states of the microresonator respectively (State I : a  
 185 Möbius-like microcavity, State V : a Fabry–Pérot resonator, State IX : a MRR). The spectra with black wireframe  
 186 represent the transition states between three states. The top left panel shows the simulated fundamental TM mode  
 187 profile ( $n_g \sim 2.1099$ ) and the reflectivity versus the applied phase shift, derived from all the measured spectra.

### 188 3.3 Mode Splitting and Avoided Mode Crossing

189 To gain a more insightful understanding of the underlying physics governing the spectral evolution  
 190 and mode splitting, we perform comprehensive analysis using the TCMT. As a more fundamental  
 191 view of the light interaction, this model focuses on the *equivalent* between clockwise (CW) and

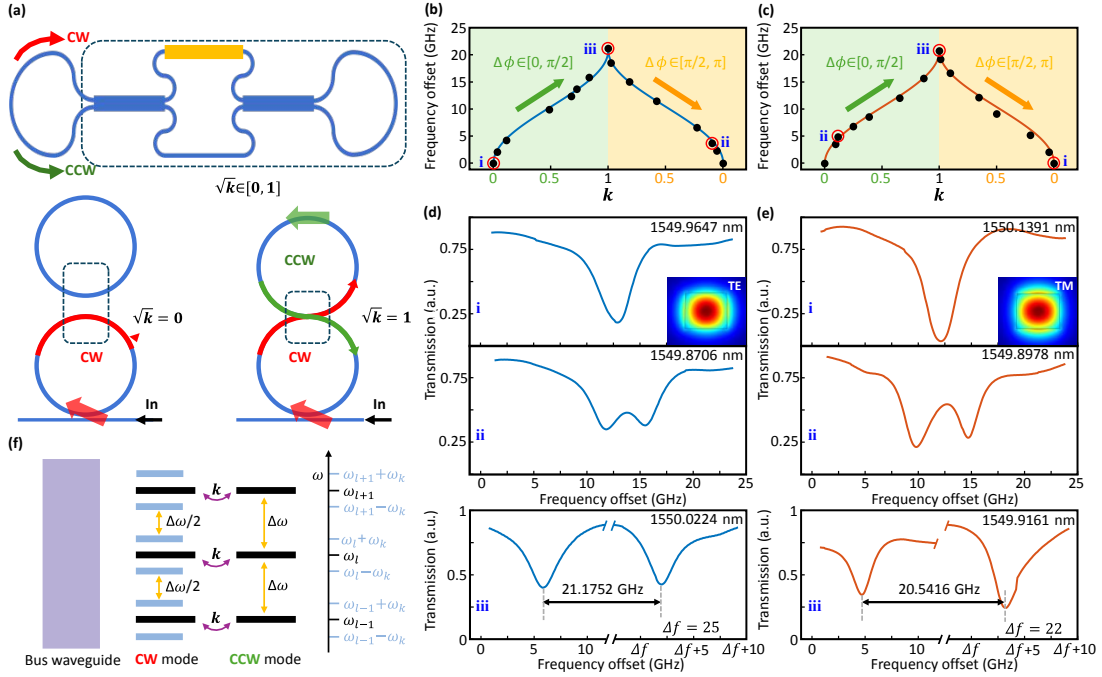
192 counterclockwise (CCW) traveling waves within the chip-scale resonator. To simplify the analysis  
 193 of optical field interactions within the microresonator, the propagation paths of CW and CCW  
 194 waves can be considered separately. For any non-zero reflectivity (where  $\Delta\phi$  is not an integer  
 195 multiple of  $\pi$ ), CW and CCW waves coexist within the resonator, as they can be converted into  
 196 each other via the phase difference between the two arms of the Sagnac reflector (a CW wave  
 197 entering the Sagnac reflector is reflected as a CCW wave, and vice versa). Because these two  
 198 modes propagate along the same physical path, the impact of the CW and CCW waves on the  
 199 transmission spectrum is equivalent to that of dual rings of equal length, where the loop  
 200 circumference corresponds to the total optical path of the reconfigurable microresonator. The  
 201 coupling efficiency between the two propagation modes is thus equivalent to the normalized  
 202 reflectivity  $R$  of the Sagnac reflector (i.e.,  $k = R(\lambda)/R_{max}$ ). When  $k=0$ , the two MRRs are completely  
 203 decoupled, corresponding to the case where  $\Delta\phi$  is an integer multiple of  $\pi$ . When  $k=1$ , the two  
 204 MRRs are fully coupled, and the optical path length becomes twice the original, resulting in a  
 205 halved FSR when  $\Delta\phi = \pi/2$ . The mode splitting in intermediate states can be quantitatively analyzed  
 206 using the dual-ring mode coupling theory:

$$\Delta f_n = \frac{1}{\pi} \frac{\theta_n}{T_{RT}} \quad (1)$$

207 where  $\Delta f_n$  represent the frequency difference between the two super modes corresponding to the  
 208  $n$ -th azimuthal mode number,  $\theta_n$  is the coupling rotation angle, related to the power coupling  
 209 coefficient  $kn$  by  $\theta_n = \arcsin(kn)$ , and  $T_{RT}$  denotes the cavity round-trip time. More details are be  
 210 found in S2 in the Supplementary Material.

211 We validate that the experimental mode splitting evolution for both polarizations during device  
 212 reconfiguration aligns precisely with the TCMT predictions. As shown in Fig. 6(b), the resonant  
 213 frequency difference exhibits a direct dependence on the inter-ring coupling strength ( $k$ ). The  
 214 transmission spectrum of the microresonator is shown in Fig. 6(d). At zero coupling (State i), a  
 215 single resonance dip occurs near 1549.96 nm with the typical Lorentzian lineshape. With  
 216 increasing  $k$  in State ii, hybridized supermodes emerge through enhanced CW-CCW mode  
 217 coupling, generating observable mode splitting. This culminates in State iii ( $\Delta\phi = \pi/2$ ,  $k$  is  
 218 maximized), where maximal splitting yields two distinct resonances separated by approximately  
 219 21.175 GHz – effectively halving the FSR in State i. Similar behavior is observed for TM  
 220 polarization in Fig. 6(c), with a maximum frequency splitting of 20.541 GHz. This tunable dual-  
 221 mode system constitutes a prevailing photonic molecule,<sup>22</sup> demonstrating analogs to canonical

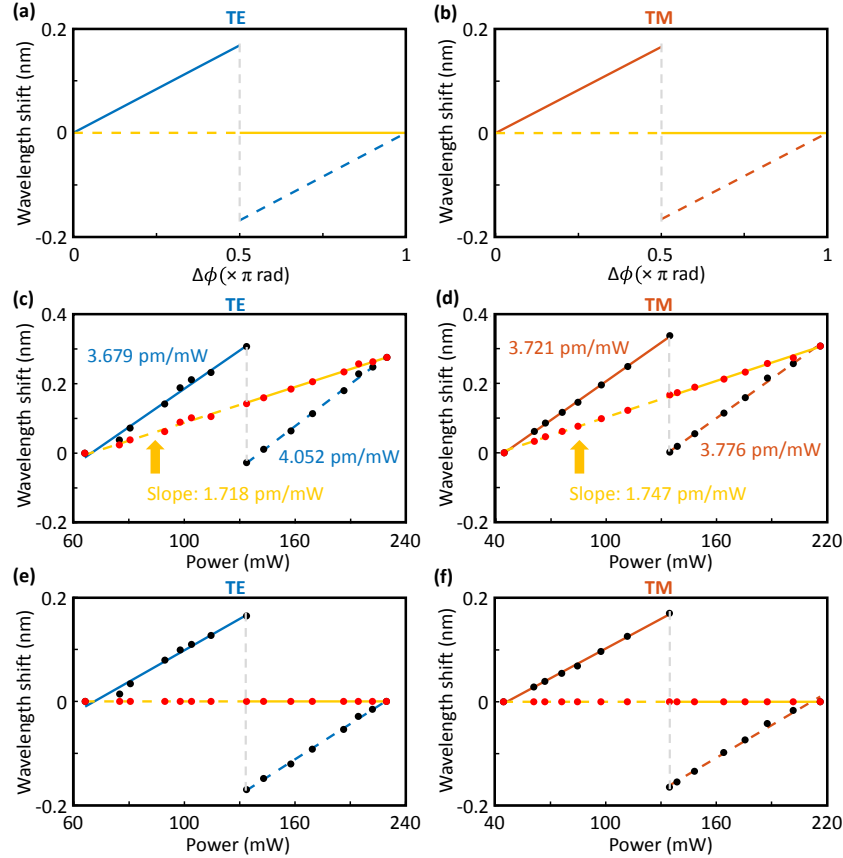
222 two-level quantum systems such as Autler-Townes splitting. Figure 6(f) accordingly illustrates the  
 223 corresponding energy-level diagram for CW and CCW modes,<sup>23</sup> with the dynamically controlled  
 224 spectral response establishing a reconfigurable platform that emulates artificial atom- and  
 225 molecule-like systems.



226 Fig. 6 (a) The schematic of the tunable dual-cavity system supporting CW and CCW modes; the equivalent dual-ring  
 227 system when  $k=0$  or  $1$ . Measured resonant frequency difference (black points) with theoretical curve fit for (b) the  
 228 fundamental TE (blue line) and (c) the fundamental TM mode (orange line). Distinctive resonance profiles  
 229 corresponding to States i, ii, and iii for (d) the fundamental TE mode and (e) the fundamental TM mode. (f) Energy-  
 230 level diagram illustration of the mode splitting with the largest coupling.  
 231

232 We demonstrate the dual polarization photonic pinning effect enabled by phase-compensated  
 233 tunable coupling. In conventional mechanical tuning methods,<sup>24,25</sup> which modulate coupling  
 234 strength solely through inter-resonator gap adjustment, the hybridized even and odd supermodes  
 235 shift simultaneously in opposite directions within the frequency domain.<sup>26</sup> By contrast, our  
 236 interferometric coupler tuning approach introduces a compensatory phase term that precisely  
 237 counteracts mode splitting dynamics. Consequently, one supermode remains frequency-pinned, as  
 238 validated theoretically and experimentally below (See S2 in the Supplementary Material for more  
 239 details). Figures 7(a–b) present numerically simulated relative resonant wavelengths of the two  
 240 supermodes as a function of the applied phase difference  $\Delta\phi$  (in units of  $\pi$  radians) under TE and  
 241 TM polarized inputs. For  $0 < \Delta\phi < 0.5\pi$ , the odd supermode (out-of-phase state) remains pinned at a

242 fixed wavelength, while the resonant wavelength of the even supermode (in-phase state) shifts  
 243 linearly with  $\Delta\phi$ . For  $0.5\pi < \Delta\phi < \pi$ , the behavior of the two supermodes is reversed: the odd  
 244 supermode now shifts linearly with the phase, while the even supermode becomes wavelength-  
 245 pinned.



246 Fig. 7 Wavelength shift of the resonant supermodes as a function of the applied phase difference ( $\Delta\phi$ , in units of  $\pi$   
 247 radians) for (a) TE and (b) TM polarized inputs. Where solid lines (dashed lines) represent the even supermode (odd  
 248 supermode). Experimental resonance wavelength offset under varying applied power for (c) TE and (d) TM  
 249 polarizations. Data points (black and red circles) correspond to measured resonance (even and odd modes) positions,  
 250 and solid lines (blue/orange and yellow) indicate linear fits. Separating the thermal crosstalk from the experimental  
 251 data of (e) TE and (f) TM polarizations by subtracting the shift of the pinning mode from all three wavelength shifts.  
 252

253 In addition to phase-sensitive coupling variations, the thermal tuning approach introduces  
 254 thermal crosstalk,<sup>27</sup> that inevitably increasing the cavity length and causing a red shift in the  
 255 spectra. The measured resonant wavelength offsets under varying applied electrical power for TE  
 256 and TM polarizations are shown in Figs. 7(c-d). The actual trendlines of photonic pinned  
 257 supermodes are slightly titled. Yellow lines represent the linear least-squares fits to the  
 258 experimental data (red solid dots). Therefore, the thermal crosstalk values are derived as 1.718

259 pm/mW for TE polarization and 1.747 pm/mW for TM polarization, indicating consistent and  
260 polarization-insensitive thermal response. Furthermore, we subtract the shift of the pinning mode  
261 from all three wavelength shifts to separate the crosstalk term from the experimental data. The  
262 results after separation are shown in Figs. 7(e–f), which exhibit excellent agreement with the  
263 simulation results. This indicates that if the impact of thermal crosstalk on the device can be further  
264 mitigated, for example, by introducing thermal isolation trenches around the electrodes, the photon  
265 pinning phenomenon could be directly observed from the spectral response. Notably, the MEMS  
266 tuning approach<sup>28</sup> not only enables a non-thermal method for crosstalk tuning but also delivers  
267 ultra-low static tuning power, addressing key limitations of conventional thermal tuning strategies.  
268 This pinning phenomenon is analogous to avoided mode crossing (AMX)-induced Kerr comb  
269 generation.<sup>29,30</sup> By controlling AMX location, initial comb lines can be selectively generated at  
270 specified resonances, facilitating repetition-rate-selectable combs. As the representative behavior  
271 of photonic molecules,<sup>3,31</sup> the AMX has also been widely explored in both classical and quantum  
272 scenarios.<sup>32-34</sup> The observed photonic pinning effect underscores the rich physical dynamics  
273 underlying our reconfigurable microresonator.

#### 274 **4 Conclusion**

275 To sum up, we propose and experimentally demonstrate a versatile reconfigurable integrated Si<sub>3</sub>N<sub>4</sub>  
276 photonic microresonator that fundamentally expands the capabilities of on-chip devices. We  
277 successfully show that a single device can dynamically transition through three major operational  
278 modes—a Möbius-like cavity, a Fabry-Pérot resonator, and a standard microring resonator—a  
279 behavior that is accurately modeled using the TMM and intuitively explained by the TCMT.  
280 Beyond comprehensive demonstration of reconfigurability, our experiments reveal several  
281 surprising phenomena. We show that the device can achieve FSR multiplication by leveraging a  
282 unique photonic router topology, where the FSR is halved as a direct result of twice the optical  
283 path before constructive interference. Furthermore, we observe a dual-polarization photonic  
284 pinning effect enabled by phase-compensated tuning, which allows one supermode to remain  
285 frequency-pinned. The size of standard photonic components inside can be significantly reduced  
286 by inversely designed methods,<sup>35,36</sup> contributing to a more compact footprint. This phenomenon  
287 has potential implications for photonic systems, demonstrating analogs to canonical two-level  
288 quantum systems and offering a route for realizing artificial atom- and molecule-like systems<sup>37</sup>

289 and synthetic dimensions<sup>38-42</sup> on a chip. The demonstrated ability to achieve multi-functionality  
290 and rich physical phenomena on a single platform represents a significant step towards advanced  
291 programmable photonic system-on-chip.

292

### 293 **Disclosures**

294 The authors declare no conflicts of interest.

295

### 296 **Code and Data Availability**

297 The data that support the findings of this study are available from the corresponding author on  
298 reasonable request.

299

### 300 *Acknowledgments*

301 This research was supported by the National Natural Science Foundation of China (NSFC) (Grant  
302 Nos. 62105061, 12374301, and 62225404); Jiangsu Provincial Frontier Technology Research and  
303 Development Program (Grant No. BF2024070); the National Key R&D Program of China (Grant  
304 No. 2024YFA1210500); the Key Lab of Modern Optical Technologies of Education, Ministry of  
305 China, Soochow University. The authors thank Yong Xu for insightful discussion.

306

307 **Tong Lin** is an associate professor at the Southeast University. He received his BS degree in optics  
308 from the Zhejiang University in 2012, and his PhD degree in mechanical engineering from the  
309 National University of Singapore in 2016. He is the author of more than 50 journal papers. His  
310 current research interests include silicon nitride photonics, frequency comb, optical interconnects,  
311 silicon photonics, metrology, and optoelectronic systems. He is a member of SPIE.

312

313 Biographies and photographs for the other authors are not available.

314

### 315 **Caption List**

316

317 **Fig. 1** The artistic view of the proposed reconfigurable dual-polarization Si<sub>3</sub>N<sub>4</sub> microresonator,  
318 supporting three distinctive resonators.

319 **Fig. 2** (a) The schematic of the tunable Sagnac reflector as the photonic router ( $L_{\text{MMI}}=130 \mu\text{m}$ ).  
320 The inset is one optical microscope image of the fabricated MMI. (b) Simulated two port  
321 transmission spectra of a polarization-insensitive MMI for TE mode (blue line) and TM mode  
322 (orange line). (c) Simulated reflection and transmission spectra of the constructed Sagnac reflector  
323 for TE mode (blue line) and TM mode (orange line).

324 **Fig. 3** The optical microscope image of the fabricated device and the experimental apparatus for  
325 characterizing its optical properties: TSL (Santec TLS-570), PC (Polarization controller), DC  
326 power supply (Keysight 33522B), P (OPPF05-NIR, JCOPTIX), PD (Santec MPM-210).

327 **Fig. 4** The spectral evolutions of the reconfigurable  $\text{Si}_3\text{N}_4$  microresonator for TE-polarized input  
328 with the wavelength spanning from 1549 nm to 1551 nm by altering the applied electrical power  
329 (P). Among them, the red, green, and blue bold wireframe correspond to three distinct states of the  
330 microresonator (i.e., State **I** : a Möbius-like microcavity, State **V** : a Fabry-Pérot resonator, and  
331 State **IX**: a MRR ). The spectra with black wireframe represent the transition states between three  
332 states. The top left panel shows the simulated fundamental TE mode profile ( $n_g \sim 2.0863$ ) and the  
333 reflectivity versus the applied phase shift, derived from all the measured spectra.

334 **Fig. 5** The spectral evolutions of the reconfigurable  $\text{Si}_3\text{N}_4$  microresonator for the TM-polarized  
335 input with the wavelength spanning from 1549 nm to 1551 nm by altering the applied electrical  
336 power (P). Among them, the red, green, and blue bold wireframe correspond to three distinct states  
337 of the microresonator (i.e., State **I** : a Möbius-like microcavity, State **V** : a Fabry-Pérot resonator,  
338 and State **IX**: a MRR ). The spectra with black wireframe represent the transition states between  
339 three states. The top left panel shows the simulated fundamental TM mode profile ( $n_g \sim 2.1099$ ) and  
340 the reflectivity versus the applied phase shift, derived from all the measured spectra.

341 **Fig. 6** (a) The schematic of the tunable dual-cavity system supporting CW and CCW modes; the  
342 equivalent dual-ring system when  $k=0$  or  $1$ . Measured resonant frequency difference (black points)  
343 with theoretical curve fit for (b) the fundamental TE (blue line) and (c) the fundamental TM mode  
344 (orange line). Distinctive resonance profiles corresponding to States i, ii, and iii for (d) the  
345 fundamantal TE mode and (e) the fundamantal TM mode. (f) Energy-level diagram illustration of  
346 the mode splitting with the largest coupling.

347 **Fig. 7** Wavelength offset of the resonant supermodes as a function of the applied phase difference  
348 ( $\Delta\phi$ , in units of  $\pi$  radians) for (a) TE and (b) TM polarized inputs. Where solid lines (dashed lines)  
349 represent the even supermode (odd supermode). Experimental resonance wavelength shift under

350 varying applied power for (c) TE and (d) TM polarizations. Data points (black and red circles)  
351 correspond to measured resonance (even and odd modes) positions, and solid lines (blue/orange  
352 and yellow) indicate linear fits. Separating the thermal crosstalk from the experimental data of (e)  
353 TE and (f) TM polarizations by setting the offset of the pinning mode to zero.

#### 354 *References*

- 355 1. Wim Bogaerts, Daniel Pérez, José Capmany, David A. B. Miller, Joyce Poon, Dirk Englund,  
356 Francesco Morichetti & Andrea Melloni , “Programmable photonic circuits,” *Nature* 586(7828), 207–  
357 216 (2020)[doi:10.1038/s41586-020-2764-0].
- 358 2. Fu Feng, Dewang Huo, Ziyang Zhang, Yijie Lou, Shengyao Wang, Zhijuan Gu, Dong-Sheng Liu,  
359 Xinhui Duan, Daqian Wang, Xiaowei Liu, Ji Qi, Shaoliang Yu, Qingyang Du, Guangyong Chen,  
360 Cuicui Lu, Yu Yu, Xifeng Ren, Xiaocong Yuan, “Symbiotic evolution of photonics and artificial  
361 intelligence: a comprehensive review,” *Adv. Photon.* 7(2), 024001 (2025)  
362 [doi:10.1117/1.AP.7.2.024001].
- 363 3. Zihan Tao, Bitao Shen, Wencan Li, Luwen Xing, Haoyu Wang, Yichen Wu, Yuansheng Tao, Yan  
364 Zhou, Yandong He, Chao Peng, Haowen Shu & Xingjun Wang, “Versatile photonic molecule switch  
365 in multimode microresonators,” *Light Sci. Appl.* 13(1), 51 (2024) [doi:10.1038/s41377-024-01399-  
366 0].
- 367 4. Yufei Wang, Kun Liao, Kuo Zhang, Zhuochen Du, Ze Wang, Bo Ni, Tianyu Xu, Shuai Feng, Yan  
368 Yang, Qi-Fan Yang, Quan Sun, Xiaoyong Hu & Qihuang Gong , “Reconfigurable versatile integrated  
369 photonic computing chip,” *eLight* 5 (1), 20(2025) [doi:10.1186/s43593-025-00098-6].
- 370 5. Maoliang Wei, Junying Li, Zequn Chen, Bo Tang, Zhiqi Jia, Peng Zhang, Kunhao Lei, Kai Xu,  
371 Jianghong Wu, Chuyu Zhong, Hui Ma, Yuting Ye, Jialing Jian, Chunlei Sun, Ruonan Liu, Ying Sun,  
372 Wei. E. I. Sha, Xiaoyong Hu, Jianyi Yang, Lan Li, Hongtao Lin, “Electrically programmable phase-  
373 change photonic memory for optical neural networks with nanoseconds in situ training capability,”  
374 *Adv. Photon.* 5(4), 046004 (2023)[doi:10.1117/1.AP.5.4.046004].

- 375 6. Jin Li, Min Tang, Xiaoyu Wang, Christian N. Saggau, Yin Yin, Libo Ma, Qinghai Song, Oliver G.  
376 Schmidt, Jiawei Wang, “Reconfigurable resonance trapping in single optical microresonators,”  
377 *Newton* 100171(2025) [doi:10.1016/j.newton.2025.100171].
- 378 7. Aseema Mohanty, Qian Li, Mohammad Amin Tadayon, Samantha P Roberts, Gaurang R Bhatt,  
379 Euijae Shim, Xingchen Ji, Jaime Cardenas, Steven A Miller, Adam Kepecs, Michal Lipson,  
380 “Reconfigurable nanophotonic silicon probes for sub-millisecond deep-brain optical stimulation,”  
381 *Nat. Biomed. Eng.* 4 (2), 223–231 (2020) [doi:10.1038/s41551-020-0516-y].
- 382 8. Yiming Pang, Joshua E. Castro, Trevor J. Steiner, Liao Duan, Noemi Tagliavacche, Massimo Borghi,  
383 Lillian Thiel, Nicholas Lewis, John E. Bowers, Marco Liscidini, and Galan Moody, “Versatile chip-  
384 scale platform for high-rate entanglement generation using an AlGaAs microresonator array,” *PRX*  
385 *Quantum* 6(1), 010338 (2025) [doi:10.1103/PRXQuantum.6.010338].
- 386 9. Daniel Pérez-López, Ana Gutierrez, David Sánchez, Aitor López-Hernández, Mikel Gutierrez, Erica  
387 Sánchez-Gomáriz, Juan Fernández, Alejandro Cruz, Alberto Quirós, Zhenyun Xie, Jesús Benitez,  
388 Nandor Bekesi, Alejandro Santomé, Diego Pérez-Galacho, Prometheus DasMahapatra, Andrés  
389 Macho, José Capmany, “General-purpose programmable photonic processor for advanced  
390 radiofrequency applications,” *Nat. Commun.* 15(1), 1563 (2024) [doi:10.1038/s41467-024-45888-7].
- 391 10. Jun Dong, “Double injection resonator,” *Nat. Photon.* 12(11), 642–644 (2018) [doi:10.1038/s41566-  
392 018-0286-1].
- 393 11. Roei Aviram Cohen, Ofer Amrani & Shlomo Ruschin, “Response shaping with a silicon ring  
394 resonator via double injection,” *Nat. Photon.* 12(12), 706–712 (2018) [doi:10.1038/s41566-018-0275-  
395 4].
- 396 12. Xin Guo, Yang Liu, Tangman Yin, Blair Morrison, Mattia Pagani, Okky Daulay, Wim Bogaerts,  
397 Benjamin J. Eggleton, Alvaro Casas-Bedoya, David Marpaung, “Versatile silicon microwave  
398 photonic spectral shaper,” *APL Photon.* 6(3), 016101(2021) [doi:10.1063/5.0033516].

- 399 13. Ming Chen, Yifan Liu, Kaixiang Cao, Yuan Yu, Fangzheng Zhang, Xinliang Zhang, “Ultrahigh  
400 rejection microring resonator assisted by an all-pass filter,” *Adv. Photon.Nexus* 3(6), 066011 (2024)  
401 [doi:10.1117/1.APN.3.6.066011].
- 402 14. Zheru Qiu, Neetesh Singh, Yang Liu, Xinru Ji, Rui Ning Wang, Franz X. Kärtner, and Tobias  
403 Kippenberg, “Large-scale photonic chip based pulse interleaver for low-noise microwave  
404 generation,” *Nat. Commun.* 16(1), 5252 (2025) [doi:10.1038/s41467-025-59794-z].
- 405 15. Chuangchuang Wei, Hanke Feng, Kaixuan Ye, Maarten Eijkel, Yvan Klaver, Zhaoxi Chen, Akshay  
406 Keloth, Cheng Wang&David Marpaung, “Programmable multifunctional integrated microwave  
407 photonic circuit on thin-film lithium niobate,” *Nat. Commun.* 16(1), 2281 (2025)  
408 [doi:10.1038/s41467-025-57441-1].
- 409 16. Dong Liang, Ahmad W. Mohammad, Chris Roeloffzen, Qinggui Tan, Li Li, Xiaojun Li, Bin Shao,  
410 Bo Zhang, Xiangke Deng, Feiteng Zheng, Lennart Wevers, Robert Grootjans, Paul Kapteijn, Roelof  
411 Bernardus Timens, Rick Heuvink, Sami Musa, “Chip-based microwave photonic payload repeater for  
412 high throughput satellites,”*Laser Photon. Rev.* 18(2), 2200952 (2024) [doi:10.1002/lpor.202200952].
- 413 17. Pengfei Zheng, Xuemeng Xu, Guohua Hu, Ruohu Zhang, Binfeng Yun, Yiping Cui, "Integrated  
414 Multi-Functional Optical Filter Based on a Self-Coupled Microring Resonator Assisted MZI  
415 Structure," in *Journal of Lightwave Technology*, vol. 39, no. 5, pp. 1429-1437, 1 March 1, 2021, doi:  
416 10.1109/JLT.2020.3037709.
- 417 18. Xin-Biao Xu, Lei Shi, Guang-Can Guo, Chun-Hua Dong, Chang-Ling Zou, “Möbius” microring  
418 resonator. *Appl. Phys. Lett.* 11 March 2019; 114 (10): 101106.
- 419 19. Kai Wang, Zeruihong She, Hongren Tan, Tianyue Zhang, and Lei Zhang, “Computational  
420 spectrometer with multi-channel cascaded silicon add-drop micro-ring resonators,” *Opt. Lett.* 49(21),  
421 6041–6044 (2024) [doi:10.1364/OL.540134].
- 422 20. Daniel J. Blumenthal; René Heideman; Douwe Geuzebroek; Arne Leinse; Chris Roeloffzen, “Silicon  
423 nitride in silicon photonics,” *Proc. IEEE* 106(12), 2209–2231  
424 (2018)[doi:10.1109/JPROC.2018.2861576].

- 425 21. Shangqing Shi, Dongdong Lin, Pengcheng Liu, Guohua Hu, Tong Lin, Binfeng Yun, “Non-invasive  
426 delay state calibration of silicon optical switching delay line,” *J. Lightwave Technol.* 40(19), 6444–  
427 6453 (2022) [doi:10.1109/JLT.2022.3195348].
- 428 22. Mian Zhang, Cheng Wang, Yaowen Hu, Amirhassan Shams-Ansari, Tianhao Ren, Shanhui Fan &  
429 Marko Lončar, “Electronically programmable photonic molecule,” *Nat. Photon.* 13(1), 36–40  
430 (2019)[doi:10.1038/s41566-018-0317-y].
- 431 23. Yaowen Hu, Mengjie Yu, Brandon Buscaino, Neil Sinclair, Di Zhu, Rebecca Cheng, Amirhassan  
432 Shams-Ansari, Linbo Shao, Mian Zhang, Joseph M. Kahn, Marko Lončar, “High-efficiency and  
433 broadband on-chip electro-optic frequency comb generators,” *Nat. Photon.* 16(10), 679–685 (2022)  
434 [doi:10.1038/s41566-022-01059-y].
- 435 24. Tobias Siegle, Stefan Schierle, Sarah Kraemmer, Benjamin Richter, Sentayehu F Wondimu, Peter  
436 Schuch, Christian Koos, Heinz Kalt, “Photonic molecules with a tunable inter-cavity gap,” *Light Sci.*  
437 *Appl.* 6(3), e16224(2017) [doi:10.1038/lsa.2016.224].
- 438 25. Long Chang, Xiaoshun Jiang, Shiyue Hu, Chao Yang, Jianming Wen, Liang Jiang, Guanyu Li,  
439 Guanzhong Wang, Min Xiao, “Parity–time symmetry and variable optical isolation in active–passive-  
440 coupled microresonators,” *Nat. Photon.* 8(7), 524–529 (2014) [doi:10.1038/nphoton.2014.133].
- 441 26. Bo Peng, Sahin Kaya Ozdemir, Jianguang Zhu, Lan Yang, “Photonic molecules formed by coupled  
442 hybrid resonators,” *Opt. Lett.* 37(16), 3435–3437 (2012) [doi:10.1364/OL.37.003435].
- 443 27. Xiaoxiao Xue, Yi Xuan, Pei-Hsun Wang, Yang Liu, Dan E. Leaird, Minghao Qi, Andrew M. Weiner,  
444 “Normal-dispersion microcombs enabled by controllable mode interactions,” *Laser Photon. Rev.*  
445 9(4), L23–L28 (2015) [doi:10.1002/lpor.201500107].
- 446 28. Young Jae Park, Man Jae Her, Youngjae Jeong, Dong Ju Choi, Dong Uk Kim, Min Gi Lim, Myung  
447 Seok Hong, Hyug Su Kwon, Kyoungsik Yu & Sangyoon Han. Fully tunable Fabry-Pérot cavity based  
448 on MEMS Sagnac loop reflector with ultra-low static power consumption. *Microsyst Nanoeng* 10,  
449 119 (2024).

- 450 29. Xiaoxiao Xue, Yi Xuan, Yang Liu, Pei Hsun Wang, Steven Chen, Jian Wang, Dan E. Leaird,  
451 Minghao Qi, Andrew M. Weiner, “Mode-locked dark pulse Kerr combs in normal-dispersion  
452 microresonators,” *Nat. Photon.* 9(9), 594–600 (2015) [doi:10.1038/nphoton.2015.137].
- 453 30. Yang Liu, Yi Xuan, Xiaoxiao Xue, Pei Hsun Wang, Steven Chen, Andrew J. Metcalf, Jian Wang,  
454 Daniel E. Leaird, Minghao Qi, Andrew M. Weiner, “Investigation of mode coupling in normal-  
455 dispersion silicon nitride microresonators for Kerr frequency comb generation,” *Optica* 1(13), 137–  
456 144 (2014) [doi:10.1364/OPTICA.1.000137].
- 457 31. Qing-Xin Ji, Peng Liu, Warren Jin, Joel Guo, Lue Wu, Zhiquan Yuan, Jonathan Peters, Avi Feshali,  
458 Mario Panicci, John E. Bowers, Kerry J. Vahala, “Multimodality integrated microresonators using  
459 the Moiré speedup effect,” *Science* 383(6687), 1080–1083 (2024) [doi:10.1126/science.adk9429].
- 460 32. Steven A. Miller, Yoshitomo Okawachi, Sven Ramelow, Kevin Luke, Avik Dutt, Alessandro Farsi,  
461 Alexander L. Gaeta, and Michal Lipson., “Tunable frequency combs based on dual microring  
462 resonators,” *Opt. Express* 23(16), 21527–21540 (2015) [doi:10.1364/OE.23.021527].
- 463 33. Avik Dutt; Steven Miller; Kevin Luke; Alexander L. Gaeta; Paulo Nussenzevig; Michal Lipson,  
464 “Tunable squeezing using coupled ring resonators on a silicon nitride chip,” *Opt. Lett.* 41(2), 223–226  
465 (2016) [doi:10.1364/OL.41.000223].
- 466 34. Yoshitomo Okawachi, Bok Young Kim, Yun Zhao, Xingchen Ji, Michal Lipson, Alexander L. Gaeta,  
467 “Dynamic control of photon lifetime for quantum random number generation,” *Optica* 8(11), 1458–  
468 1461 (2021) [doi:10.1364/OPTICA.433102].
- 469 35. Sean Molesky, Zin Lin, Alexander Y. Piggott, Weiliang Jin, Jelena Vucković & Alejandro W.  
470 Rodriguez. Inverse design in nanophotonics. *Nature Photon* 12, 659–670 (2018).  
471 [doi:10.1038/s41566-018-0246-9].
- 472 36. Song, Chifeng & Zhang, Zhihan & Wang, Haoran & Chen, Jianan & Zhang, Keyang & Li, Liu & Lin,  
473 Tong & Chen, Shihua & Lu, Junpeng & Ni, Zhenhua. (2024). Ultracompact and broadband Si<sub>3</sub>N<sub>4</sub> Y-  
474 branch splitter using an inverse design method. *Optics Express*. 32. 46080-46089.  
475 10.1364/OE.542341.

- 476 37. Da Xu Zi-Zhao Han Yu-Kun Lu Qihuang Gong Cheng-Wei Qiu Gang Chen Yun-Feng Xiao,  
477 “Synchronization and temporal nonreciprocity of optical microresonators via spontaneous symmetry  
478 breaking,” *Adv. Photon.* 1(4), 046002 (2019) [doi:10.1117/1.AP.1.4.046002].
- 479 38. Avik Dutt, Qian Lin, Luqi Yuan, Momchil Minkov, Meng Xiao, Shanhui Fan, “A single photonic  
480 cavity with two independent physical synthetic dimensions,” *Science* 367(6473), 59–64 (2020)  
481 [doi:10.1126/science.aaz3071].
- 482 39. Lingling Fan, Kai Wang, Heming Wang, Avik Dutt, Shanhui Fan, “Experimental realization of  
483 convolution processing in photonic synthetic frequency dimensions,” *Sci. Adv.* 9(32), eadi4956  
484 (2023) [doi:10.1126/sciadv.adi4956].
- 485 40. Avik Dutt, Luqi Yuan, Ki Youl Yang, Kai Wang, Siddharth Buddhiraju, Jelena Vučković, Shanhui  
486 Fan, “Creating boundaries along a synthetic frequency dimension,” *Nat. Commun.* 13(1), 3377 (2022)  
487 [doi:10.1038/s41467-022-31140-7].
- 488 41. Sashank Kaushik Sridhar, Sayan Ghosh, Dhruv Srinivasan, Alexander R. Miller, Avik Dutt,  
489 “Quantized topological pumping in Floquet synthetic dimensions with a driven dissipative photonic  
490 molecule,” *Nat. Phys.* 20(5), 843–851 (2024) [doi:10.1038/s41567-024-02413-3].
- 491 42. Zhao-An Wang, Xiao-Dong Zeng, Yi-Tao Wang, Jia-Ming Ren, Chun Ao, Zhi-Peng Li, Wei Liu,  
492 Nai-Jie Guo, Lin-Ke Xie, Jun-You Liu, Yu-Hang Ma, Ya-Qi Wu, Xi-Wang Luo, Shuang Wang, Jian-  
493 Shun Tang, Chuan-Feng Li & Guang-Can Guo, “Versatile photonic frequency synthetic dimensions  
494 using a single programmable on-chip device,” *Nat. Commun.* 16(1), 7780 (2025)  
495 [doi:10.1038/s41467-025-63114-w].